Hydroelastic optimisation of a composite marine propeller in a non-uniform wake

X.D. He*, Y. Hong, R.G. Wang

Center for Composite Material and Structure, Harbin Institute of Technology, Harbin 150080, China

ABSTRACT

The purpose of this paper is to optimise the hydroelastic performance of a composite marine propeller to reduce vibration and dynamic stress. A hydroelasticity method based on the finite element method (FEM) coupled with computational fluid dynamics (CFD) is used to simulate the composite marine propeller in a non-uniform wake. Composite blades can be considered as a cantilever-like laminated structure experiencing an unsteady hydrodynamic load and centrifugal force. The objective of the improved design is to minimise the vibratory hub loads. The ply angle and stacking sequence are considered as the design variables. The nonlinear periodic transient responses and vibration hub loads of the composite blade are obtained by solving coupled equations using the Newton–Raphson numerical procedure. Compared to the starting design of the propeller, the optimum solution results in a 49.6–70.6% reduction of the 7/rev hub loads.

© 2011 Elsevier Ltd. All rights reserved.

1. Introduction

The superior damping characteristics and high specific strength and stiffness of fibre-reinforced composites compared to metals have resulted in the widespread use of the former in the design of many marine structures. For high-speed rotating marine propellers requiring tight vibration control and hydroelastic stability, the potential benefits of composites also play an important role in improving the dynamic performance of the structure.

In recent years, a considerable amount of research has been completed on composite marine propellers. This is due to their advantages over propellers made from traditional materials (Mouritz et al., 2001; Marsh, 2004). Earlier research on composite marine propellers was completed by Lin (1991a, 1991b) using the PSF-2 programme (a software programme for analysing the flow field of a propeller in steady and subcavitating flows) and the effective modulus method. The stress was calculated and compared with a geometrically identical isotropic metal propeller using the commercial finite element software ABAQUS. Subsequently, a coupled 3-D FEM/VLM (Vortex-lattice Methods) method was presented by Lin and his partners for analysing composite propellers in steady flow (Lin and Lin, 1997; Lee and Lin, 2004; Lin, 2005). The effects of the stacking sequence and flow condition on the thrust, pitch, stress and delamination failures of the composite blades were assessed. Recently, Young presented a coupled FEM/BEM (Boundary Element Method) approach to investigate flexible composite propellers in subcavitating and cavitating flows (Young, 2008; Liu and Young, 2009; Motley et al., 2009). The hydrodynamic performance and efficiency were improved by utilising fluid–structure interactions.

Although the BEM can better capture the flow details than VLM can, all of the above-mentioned methods are limited to the assumption that the flow is inviscid. However, marine propeller usually operates in a viscous flow and a spatially varying wake. The propeller is the most important vibratory factor in the propeller–shaft system because it has such a great mass and moment of inertia and lies on the free end of the shafting. Thus, modelling the hydroelastic vibration of a composite propeller in a non-uniform wake is particularly important in the design process. For a high-speed rotating composite propeller with N blades, high vibrations are caused by harmonic loading on the blade due to an unsteady hydrodynamic environment and highly flexible rotating blades. The N/rev forces and moments are transmitted by the propeller to the hull as a primary source of vibration. So, a direct approach for reducing these vibrations is to design the propeller to produce low vibratory hub loads (Edward, 1988).

In this paper, to clarify the hydroelastic characteristics of the composite marine propeller in the non-uniform wake, a 3-D FEM/CFD method is applied to construct the coupled matrix of interactions between the fluid and structure, and the Newton–Raphson numerical procedure is used to solve this equation. To optimise the hydroelastic performance of the composite marine propeller, different improved design schemes are presented to minimise the vibration and blade dynamic stresses by tailoring the propeller blade composite couplings.

---

* Corresponding author. Tel./fax: +86 451 86412513.
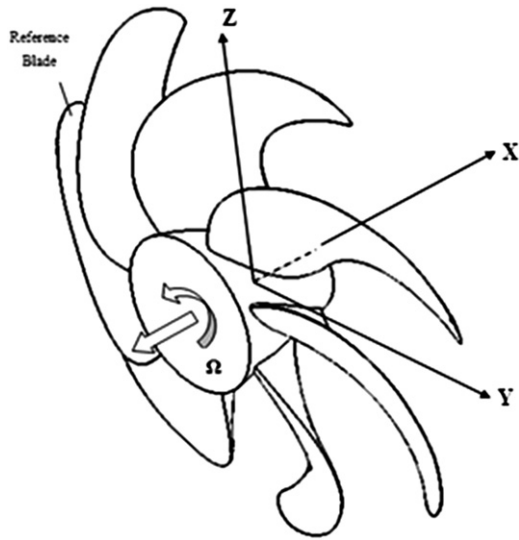 E-mail address: hrbhithy@163.com (X.D. He).

Fig. 1. Coordinate system of the composite propeller.

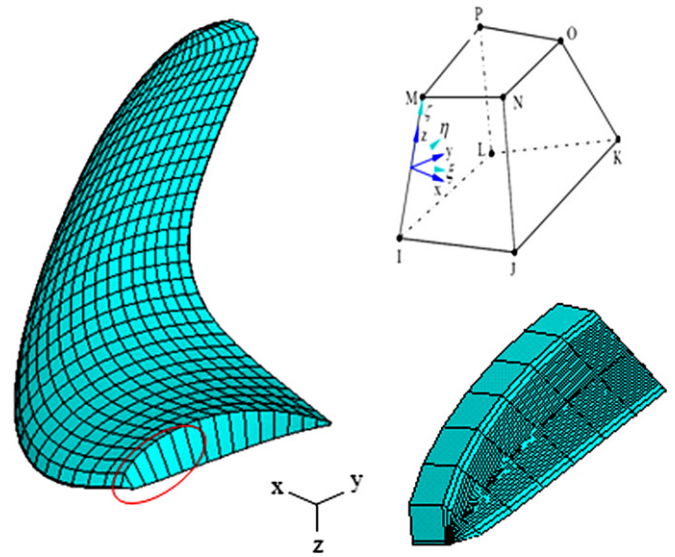Fig. 3. Finite element model of the composite blade.

Table 1
Geometry of the highly skewed propeller.

r/R	r	P/D	RK/D	SK	C/D	t/D	f/C
0.2	22	1.1209	0.0019	0	0.1882	0.0496	0.0229
0.25	27.5	1.1108	−0.0012	3.2460	0.1943	0.0456	0.0240
0.3	33	1.1028	−0.0039	5.3235	0.2009	0.0417	0.0249
0.4	44	1.0895	−0.0089	7.6465	0.2130	0.0357	0.0261
0.5	55	1.0736	−0.0143	12.4080	0.2246	0.0306	0.0268
0.6	66	1.0477	−0.0189	16.9955	0.2327	0.0268	0.0265
0.7	77	1.0044	−0.0230	21.3850	0.2336	0.0229	0.0251
0.8	88	0.9364	−0.0264	25.7265	0.2262	0.0190	0.0221
0.9	99	0.8362	−0.0295	30.1225	0.2009	0.0138	0.0162
0.95	104.5	0.7717	−0.0308	34.5510	0.1710	0.0103	0.0118
0.975	107.25	0.7354	−0.0316	36.7655	0.1290	0.0078	0.008
1	110	0.6964	−0.0323	39	0	0.0050	0

Table 2
Material properties.

Properties	UC	SC	Metal
Longitudinal modulus E_1 (Pa)	1.35e11	7.626e10	1.27e11
Transverse modulus E_2 (Pa)	9.4e9	7.626e10	
In-plane shear modulus G_{12} (Pa)	5e9	4.9e9	
In-plane Poisson's ratio v_{12}	0.28	0.32	0.42
Density ρ (kg/m^3)	1404	1536	7500

Fig. 4. Grids of the fluid computation region.

Fig. 2. Sketch of the stacking of the composite blade.
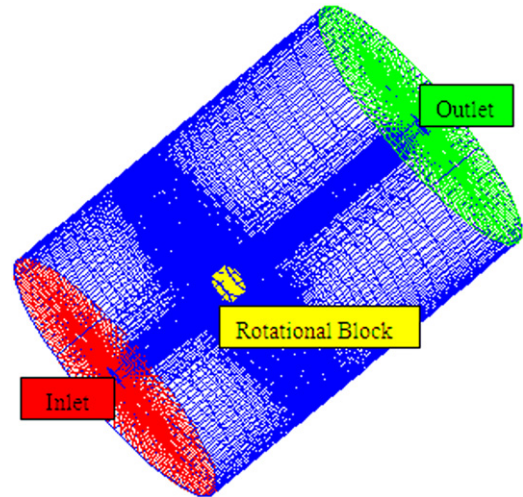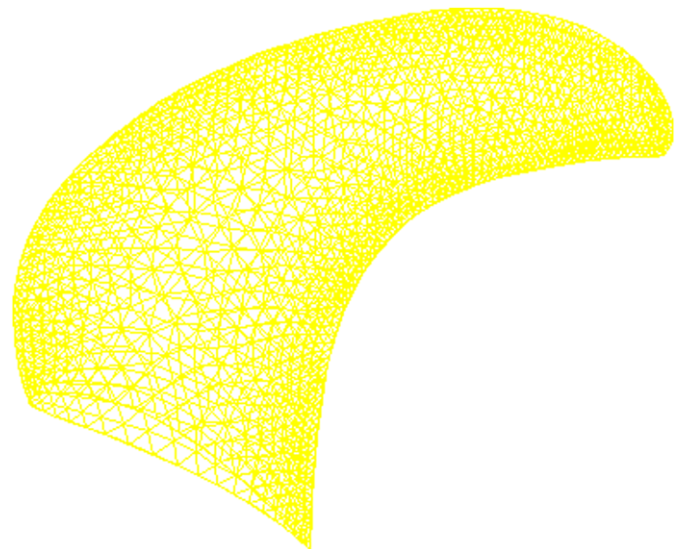

Fig. 5. Surface mesh on the composite blade.

2. Theoretical background

2.1. Dynamic analysis of a composite blade

Fig. 1 shows a composite propeller rotating with a constant angular velocity Ω about a fixed axis. The x-direction displays the
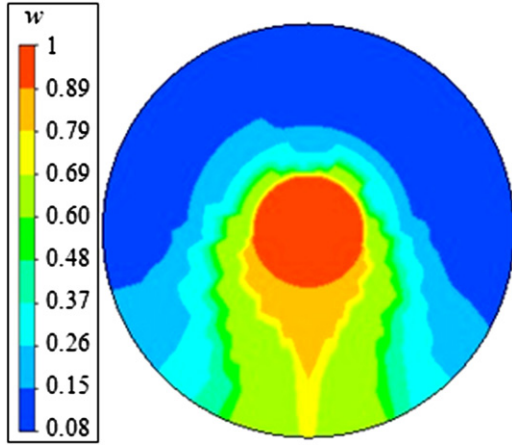

Fig. 6. Non-uniform wake distribution of the propeller.

rotational axis of the composite propeller. To analyse the hydro-elastic behaviour of the composite propeller, we choose a reference blade to construct the finite element model in the coupled matrix. The dynamic equation including the structure damping of the composite blade can be expressed as

$$[M]\{\ddot{U}\}+[C]\{\dot{U}\}+[K]\{U\}=\{F\} \qquad (1)$$

where $\ddot{U}, \dot{U}$ and U are the acceleration, velocity and displacement vectors, respectively. $[M]$, $[C]$ and $[K]$ are the mass, the damping and total stiffness matrices, respectively. The sizes of these matrices in Eq. (1) depend on the number of elements. On the right side of Eq. (1), the external load $\{F\}$ acting on the blade includes the generalised fluid force $\{F_h\}$ normal to the surface of the blade and the centrifugal force $\{F_r\}$. The force of the fluid acting on the blade can be expressed as

$$F_h = \int_A [N]^T \{m\}\{P\}dA \qquad (2)$$

where dA is the interaction boundary between the fluid and structure and m is its outward normal vector. $[N]$ is the displacement interpolation matrix, which depends on the element types used in the structural calculation. P is the total hydrodynamic pressure acting on the blade, and it can be decomposed into two parts

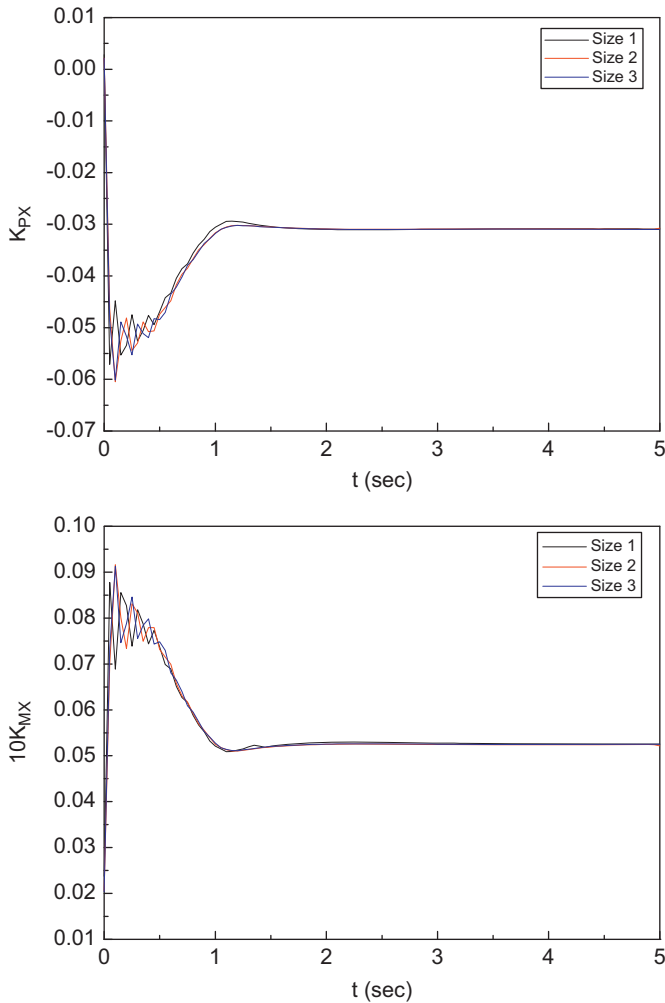$$\{P\} = \{P_r\} + \{P_v\} \qquad (3)$$

Fig. 7. Convergence of the hydrodynamic load coefficients (per blade) with grid size for the C1 blade.
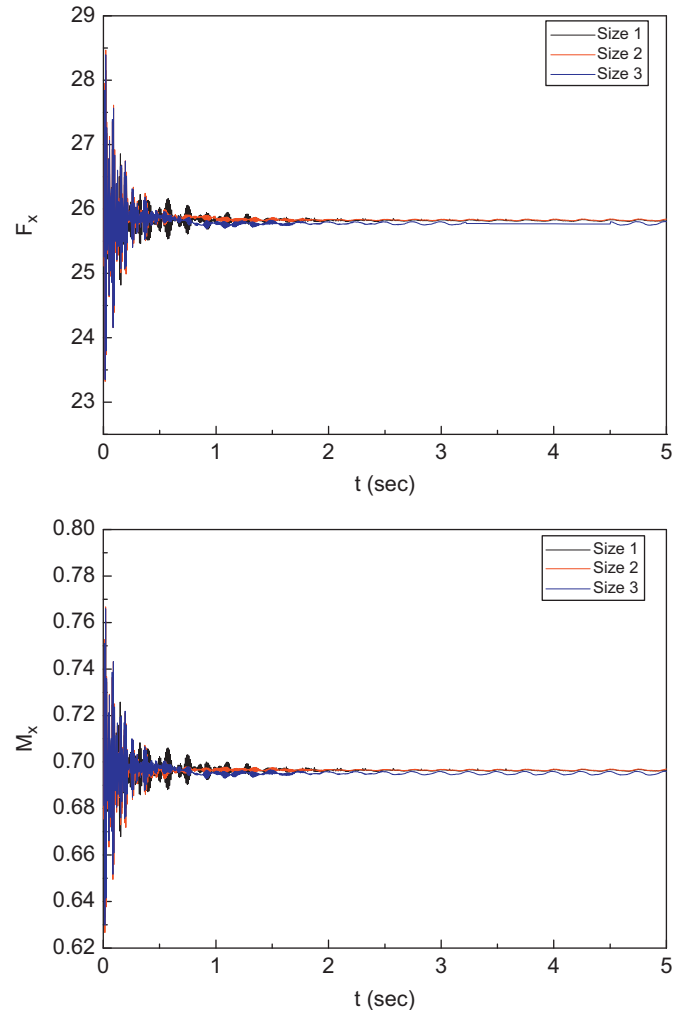

Fig. 8. Convergence of the hub force and moment with grid size for the C1 blade.

where P_r and P_v are the hydrodynamic pressure due to rotation and elastic deformation, respectively. To solve this problem, hydroelastic analysis is required.

2.2. Hydroelasticity method

The hydroelastic phenomena of a composite marine propeller in an unsteady wake are investigated using a 3-D FEM/CFD coupled method. A CFD method based on the Reynolds Averaged Navier-Stokes (RANS) equation is used for the fluid analysis in place of conventional methods (such as PSF-2, VLM and BEM), which are based on potential theory (Watanabe et al., 2003; Qing, 2002). The shear-stress transport (SST) $k-\omega$ model developed by Menter is chosen as the turbulence model (Menter, 1994). The fluid is assumed to be viscid and incompressible. With these assumptions, the hydrodynamic characteristics of the composite propeller can be obtained by applying the general-purpose CFD software CFX.

Combining Eqs. (2) and (3) with the results of the hydrodynamic pressure, the generalised fluid force $\{F_h\}$ can be considered as three parts

$$F_h(x,y,z,t) = F_h^{(1)} + F_h^{(2)} + F_h^{(3)} \tag{4}$$

where $F_h^{(1)}$, $F_h^{(2)}$ and $F_h^{(3)}$ are the hydrodynamic force, radiation force and restoring force, respectively. $F_h^{(1)}$ cannot be solved directly for incompressible fluids. However, in the CFD Solver, a Semi-Implicit Method for Pressure Linked Equations (SIMPLE) algorithm is presented for completing the coupling of pressure and velocity

and is used for solving the equations of incompressible fluids (Van Doormal and Raithby, 1984). Then, the hydrodynamic forces are obtained. $F_h^{(2)}$ and $F_h^{(3)}$ can be further expressed as

$$F_h^{(2)} = -([\overline{A}]\{\ddot{U}\} + [\overline{C}]\{\dot{U}\}) \tag{5}$$

$$F_h^{(3)} = -[\overline{B}]\{U\} \tag{6}$$

It can be seen from Eqs. (5) and (6) that the matrices $[\overline{A}]$, $[\overline{C}]$ and $[\overline{B}]$ describe the corresponding parts of hydrodynamic force that are in phase with the acceleration, velocity and displacement, respectively, of the blade vibrating in water. Thus, they are called as the added mass, added damping and added stiffness matrices, respectively. The additional mass is due to the fluid shifted by the blade as it vibrates. The added damping is due to the loss of energy through sound radiation. The added stiffness is due to the displacement of the blade vibrating.

Substituting Eqs. (4)–(6) into Eq. (1), the hydroelastic vibrating equation of the composite blade can be expressed as

$$([M] + [\overline{A}])\{\ddot{U}\} + ([C] + [\overline{C}])\{\dot{U}\} + ([K] + [\overline{B}])\{U\} = F_h^{(1)} + F_r \tag{7}$$

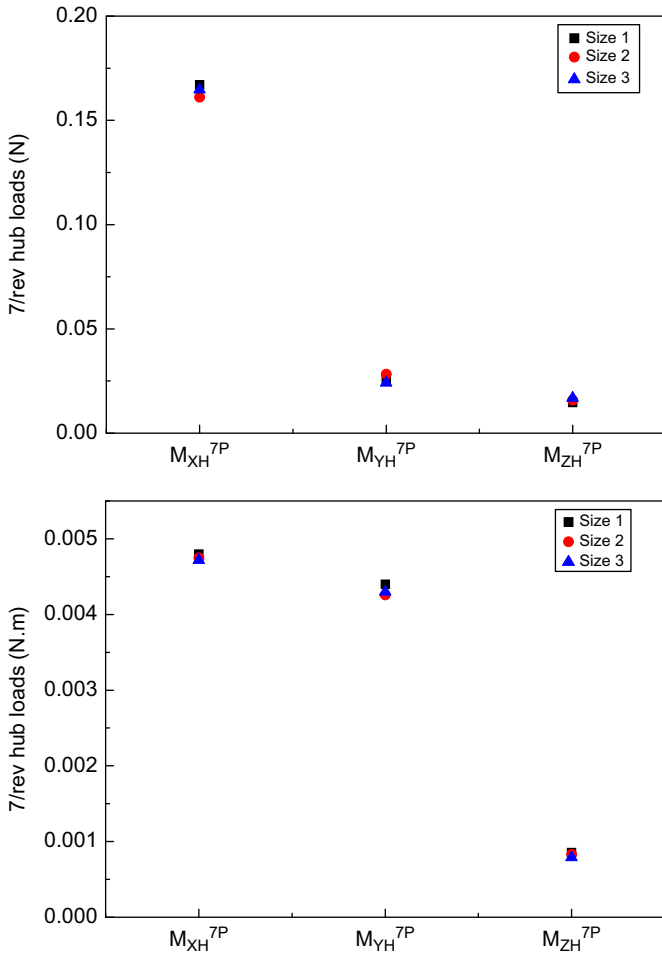The above equation can be solved with the commercial FEM/CFD software ANSYS/ANSYS CFX (ANSYS, 2009).

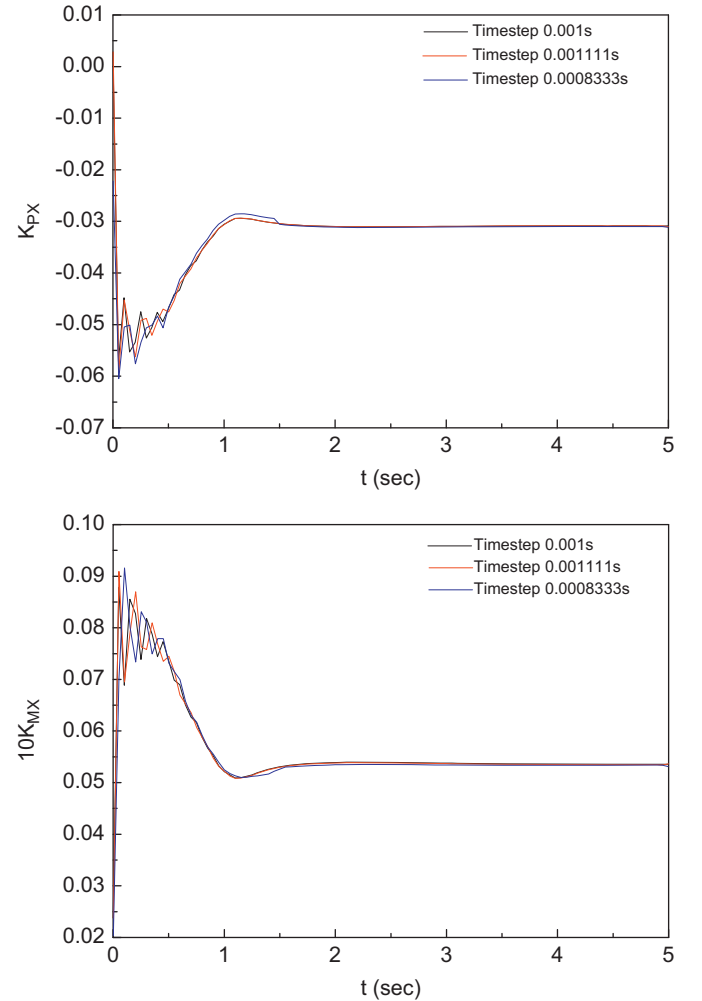Fig. 9. Convergence of 7/rev harmonic forces and moments with grid size for the C1 blade.

Fig. 10. Convergence of the hydrodynamic load coefficients (per blade) with time step size for the C1 blade.

3. Results and discussion

3.1. The numerical model

A highly skewed model propeller is analysed by applying the approach discussed above. The model propeller has seven blades, an expanded area ratio of 0.75, a diameter of 22 cm, and is made of carbon fibre-reinforced composites. Table 1 lists the geometry characteristics of the highly skewed propeller. Each composite blade can be regarded as a laminated shell with a variable cross-section and variable thickness. In this paper, the finite element model of the reference blade is made up of layered solid elements (Taylor and Beresford, 1976). We choose one element in the thickness direction of the blade, and consider each element to be a symmetric graphite-epoxy laminate composed of $0°$, $\pm 15°$, $\pm 45°$ and $90°$ plies. The propeller thickness changes as a function of position, so the number of stacking layers changes accordingly for each element. Table 2 lists the properties of the materials used in the calculation. A symmetric stacking sequence scheme $[30_2°/45_2°/0_4°/45_6°/0_6°/45_2°/0_6°]_s$ is firstly chosen for constructing the composite blade that we call the C1 blade. Fig. 2 is a sketch of the stacking orientation of the composite blade. The x-direction of the blade serves as the reference direction of the fibre. The subscript S denotes symmetry with respect to the middle surface, i.e., the camber surface, and the stacking sequence follows the order $30°$, $30°$, $45°$, $45°$, $0°$, $0°$, $0°$,… beginning from the pressure

and suction surfaces to the camber surface, respectively. The finite element model of the composite blade, generated by the software ANSYS, is shown in Fig. 3. The model consists of 510 layered solid elements. The root of the blade is fixed to simulate the boundary conditions of a real propeller blade.

A hybrid mesh is generated using the software programme GAMBIT for fluid analysis. As shown in Fig. 4, the computational domain is split into a global stationary part and a moving part, which rotates with the propeller. A simple hexahedral mesh is generated for the global stationary block, and a tetrahedral mesh is generated for the rotational block around the propeller. The detailed fluid mesh on the composite blade is shown in Fig. 5. The inlet, outlet and radial boundaries are located $4.0D$, $10.0D$ and $6.0D$ ("D" stands for diameter) away from the rotation axis at the blade generator line. The blade and hub are modelled as a solid surface, and the no slip condition is imposed. Fig. 6 shows the non-uniform wake distribution measured from model tests in a drifting condition. The wake profile is imposed using the CEL feature of CFX. A total of 335,384 cells, dividing by mesh size 1, with 139,648 cells in the rotational block and 195,736 cells in the stationary block, are used for the unsteady simulation. Another two meshing schemes, dividing by mesh size 2 and 3, are used for subsequent validation study. The total number of cells in the two cases is 157,236 and 675,248, respectively.

In summary, a coupled matrix of interaction between the fluid and the structure based on the fluid model and the finite element model is established. The Newton–Raphson numerical procedure is applied to solve this equation.
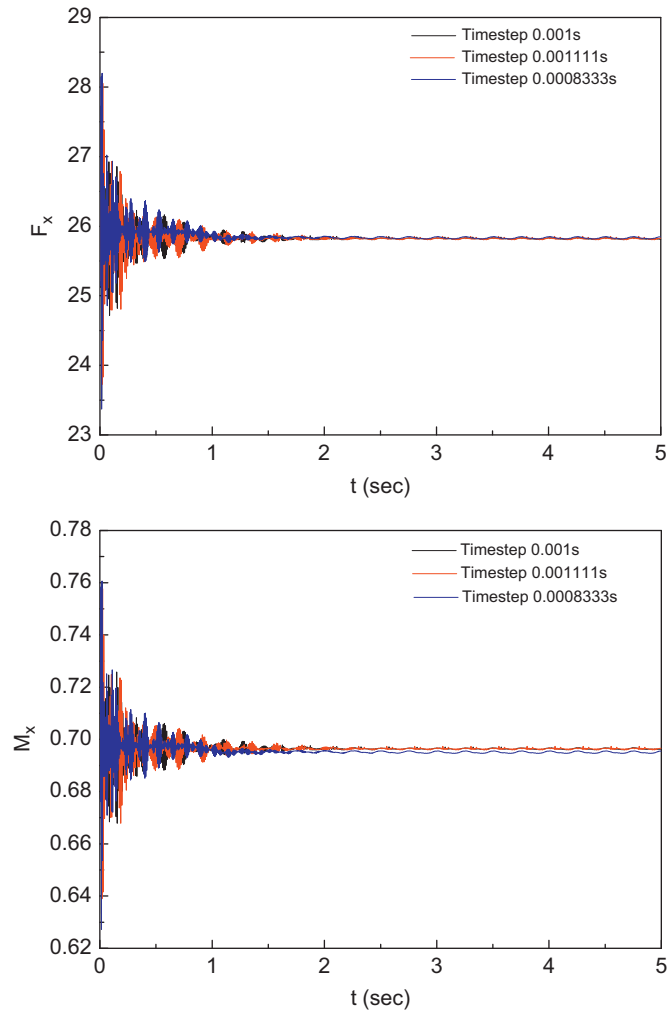

Fig. 11. Convergence of the hub force and moment with time step size for the C1 blade.
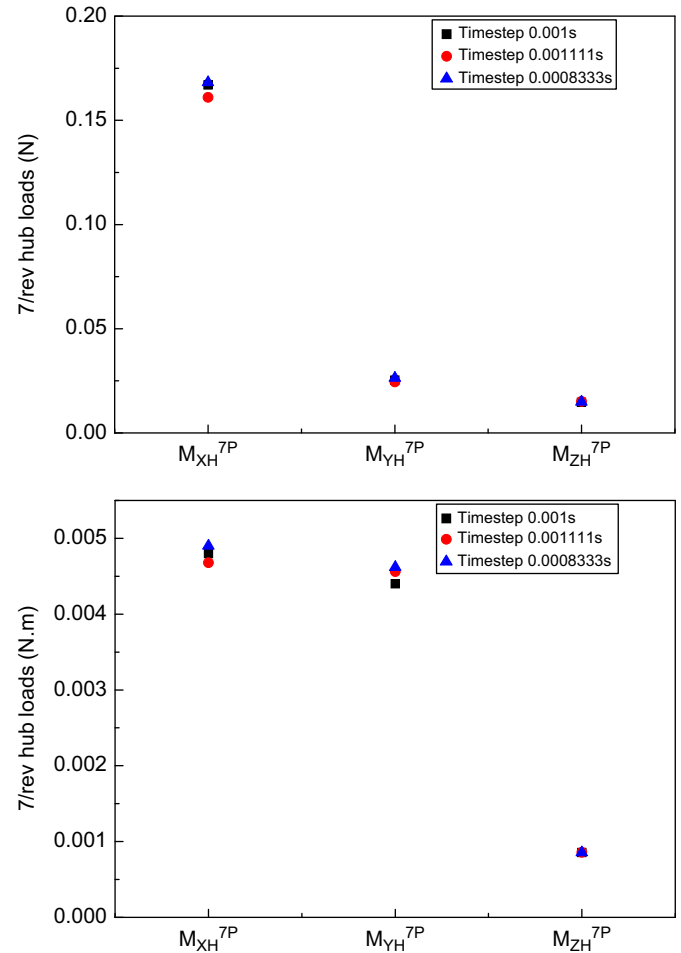

Fig. 12. Convergence of 7/rev harmonic forces and moments with time step size for the C1 blade.

3.2. Numerical validation

To confirm the validity of the 3-D FEM/CFD coupling algorithm in unsteady flows for composite propeller, the convergence calculations are completed for different grid and time step sizes. Figs. 7 and 10 show the hydrodynamic load coefficients (per blade) with grid and time step sizes, respectively. K_{PX} denotes the X component of the per blade force coefficient nondimensionalised by $\rho n^2 D^4$, K_{MX} denotes the X component of the per blade moment coefficient nondimensionalised by $\rho n^2 D^5$. Figs. 8 and 11 show the longitudinal (x direction) hub loads with grid and time step sizes, respectively. Figs. 9 and 12 present the 7/rev harmonic forces and moments of the hub loads with grid and time step sizes, respectively. We can see that the hydrodynamic load coefficients and the hub loads are convergent for different grid and time step sizes. The harmonic forces and moments of the hub loads are also convergent. The coupling method is validated for predicting the hydroelastic characteristics of the composite blade in unsteady flows.

3.3. Analysis of the hydroelastic characteristics

The hydroelastic characteristics of the composite blade subject to a non-uniform wake at the design working condition $J=0.6018$ (the advance coefficient $J = V/nD$) and $n=1200$ rpm (the rotating velocity n) are calculated using the 3-D FEM/CFD coupling algorithm. To compare the hydroelastic characteristics of the composite blade (C1 blade) with the characteristics of the metal blade, a hydroelastic analysis of the counterpart metal propeller is completed. The metal material is the traditional propeller material. Fig. 13 shows the predicted natural frequencies of the composite (C1 blade) and metal blades in water, respectively. It should be noted that the fundamental natural frequency of the composite blade in water (502 Hz) is slightly lower than that of the metal blade in water (616 Hz). That may be due to the composite blade is greatly lighter than the metal blade, the ratio between structure tonnage and structure mass increases correspondingly. So, the influence of added mass is greater for the composite blade. Also shown in this figure is the predicted mode
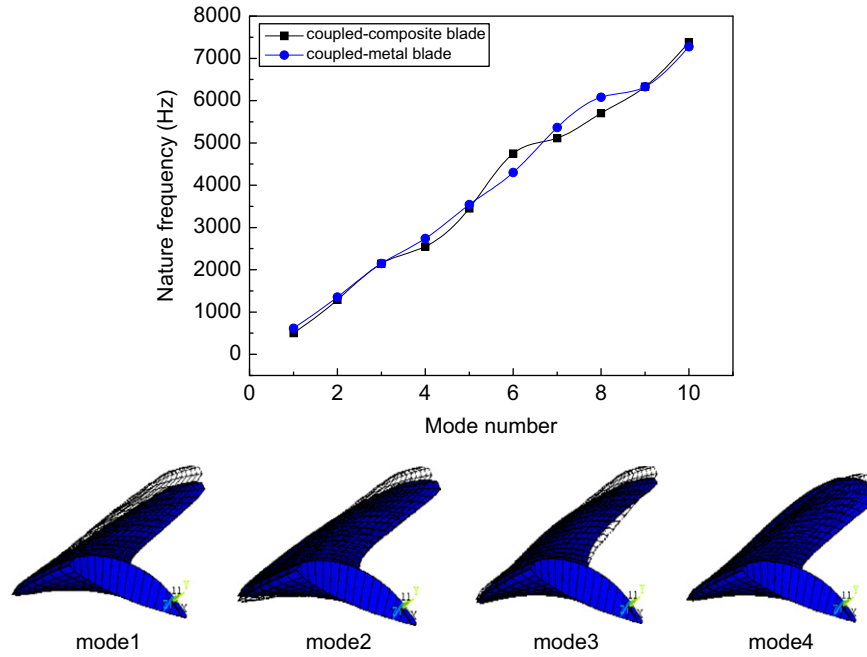

mode1   mode2   mode3   mode4

Fig. 13. Natural frequencies and mode shapes of the composite and metal blades.
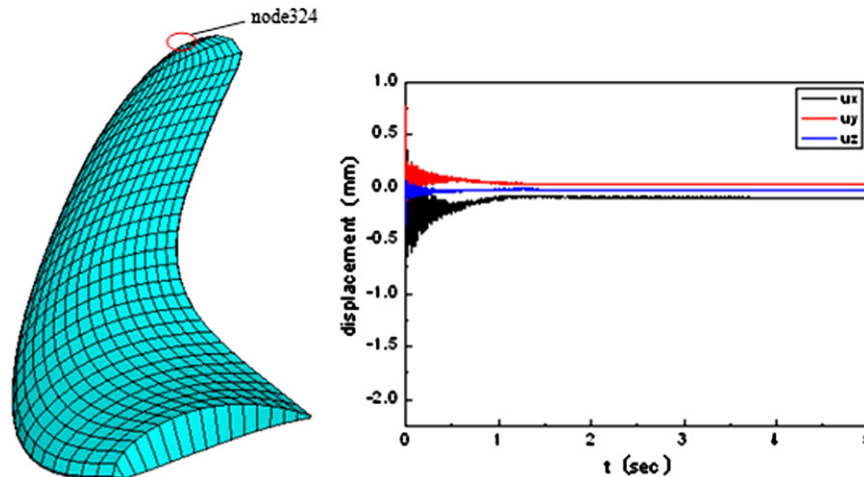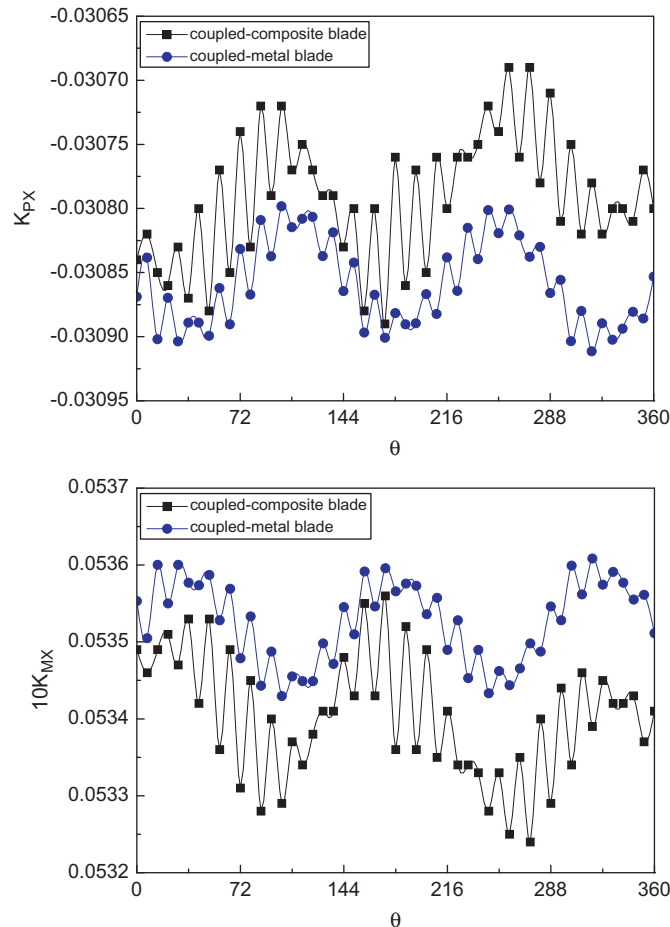

Fig. 14. Convergence curve of the displacement for the tip node of the C1 blade.
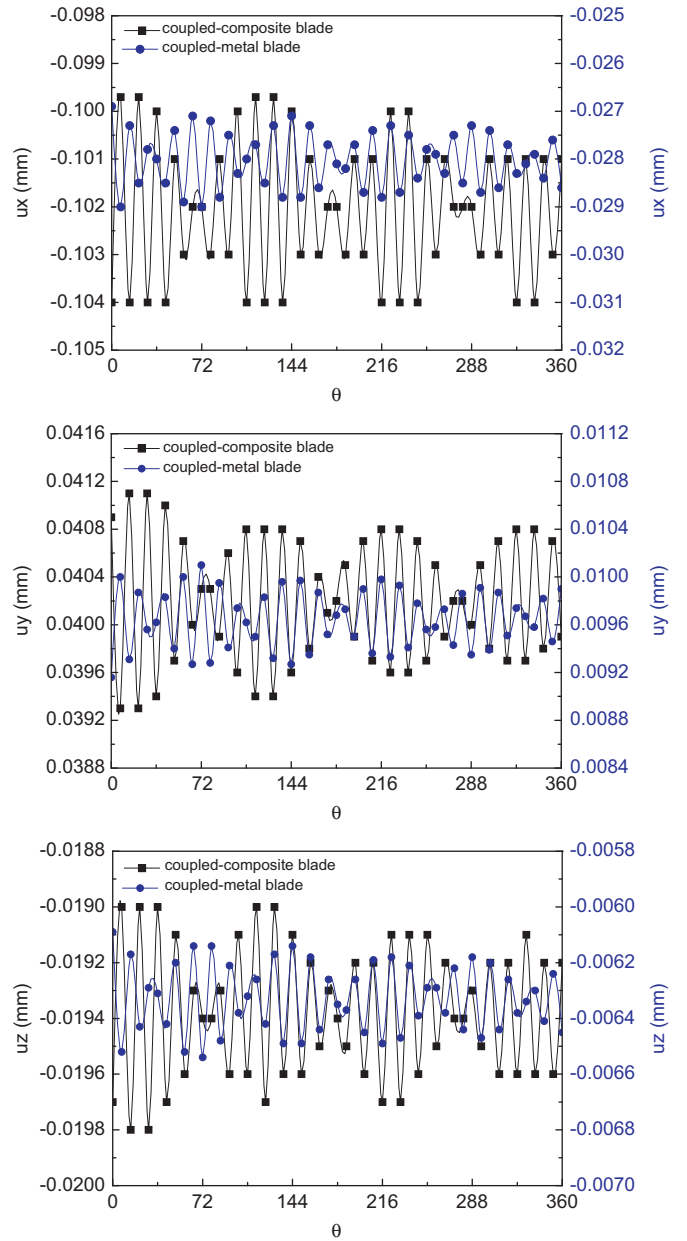
shapes of the composite and metal blades. The mode shapes of both blades are approximately the same, i.e. the first mode is the longitudinal bending mode, the second mode is the twist mode, the third and fourth modes combine these different effects.

Based on the 3-D FEM/CFD coupling algorithm, a transient calculation for a total time of 5 s was completed. The calculated time step size was set to 0.001 s. Fig. 14 shows the time-dependent displacement curves of the tip node for composite blade (C1 blade). We can see that the resistive loading of the fluid in this case results in exponential decay of the transient response.

Figs. 15–17 present the variation of the hydrodynamic load coefficients, the tip node displacement and the maximum Von-Mises stress during a rotation in non-uniform flow for the composite blade (C1 blade) and the metal blade, respectively. From these results, we can see that the data points obtained at the time step size are represented by markers. The responses between the data points have been determined by the spline interpolation. Fig. 15 shows the hydrodynamic loads of the coupled-composite blade is slightly lower than those of the coupled-metal blade, which is because that the effect of the elasticity of the composite. In Figs. 16 and 17, the left vertical axis shows the results of composite blade, and the right vertical axis shows the results of metal blade. Although the limits of these two axes are different, the ranges have been kept the same to aide with the comparison of the periodic components. The curves clearly show the oscillation characteristics of the results during a rotation for the composite and metal blades, the occurrence of these oscillations is due to the effect of the

Fig. 16. Comparisons of tip node displacement during a rotation in an unsteady flow of the composite blade (C1 blade) with that of the metal blade.

fluid-structural interaction. The hydroelastic effects of the composite blade are larger than those of the metal blade due to the favourable elasticity of the composite. The smallest oscillations occur around the rotation angles $\theta = 72$, 180 and 288 degrees for the composite blade; however, the smallest oscillations occur around the rotation angles $\theta = 36$, 108, 180, 252 and 324 degrees for the metal blade.

The harmonic loads are obtained from the time-dependent hub forces and moments of the composite and metal blades by using the FFT function in the MATLAB Toolbox (Duffy, 2003). Fig. 18 presents the longitudinal harmonic loads (x-direction) of the composite blade (C1 blade) and the metal blade. From this picture, we can see that the high frequency components of the harmonic loads are greatly lower than the 7/rev harmonic loads. The relative importance of the 7/rev harmonic loads is shown. Fig. 19 displays the vibratory hub loads (7/rev) for the composite blade (C1 blade) and the metal blade. F_{XH}^{7P}, F_{YH}^{7P} and F_{ZH}^{7P} are
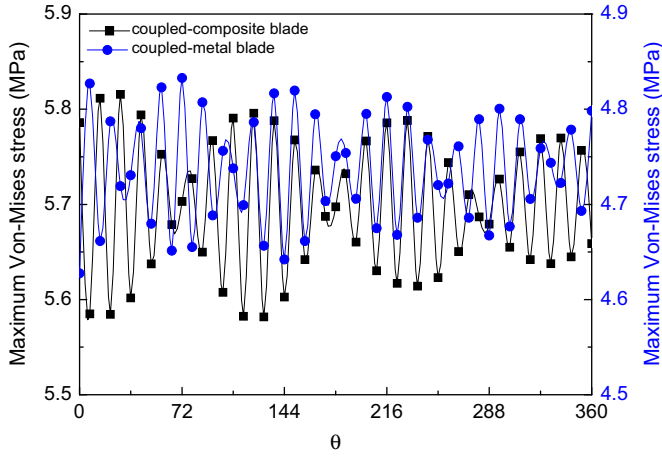

Fig. 15. Comparisons of the hydrodynamic load coefficients (per blade) during a rotation in an unsteady flow of the composite blade (C1 blade) with that of the metal blade.

Fig. 17. Comparisons of the maximum Von-Mises stress during a rotation in an unsteady flow for the composite blade (C1 blade) and the metal blade.
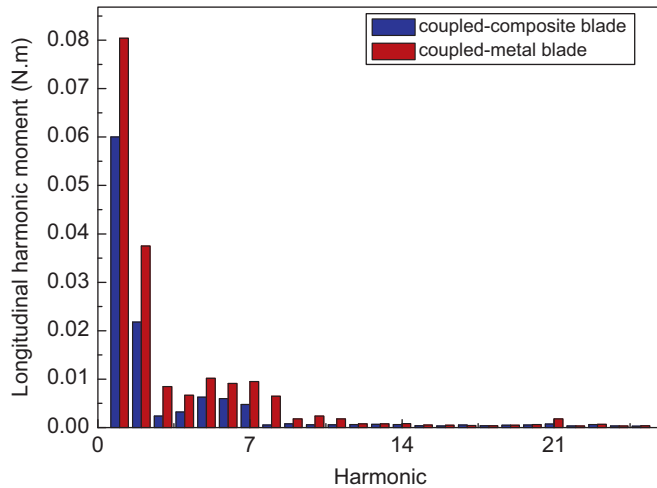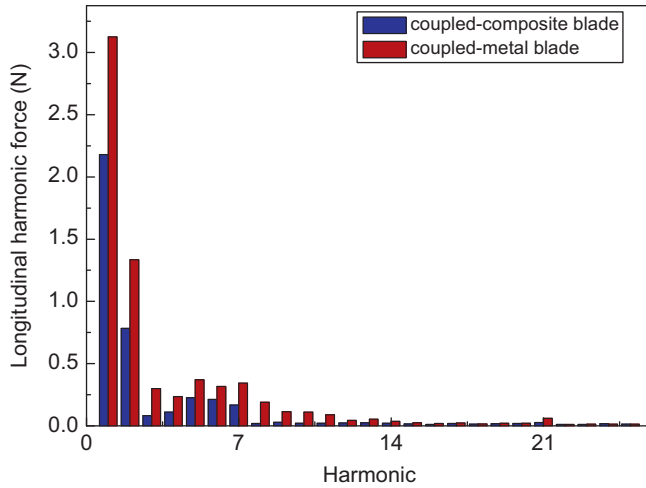

Fig. 18. Comparisons of the longitudinal harmonic loads (x-direction) for the composite blade (C1 blade) and the metal blade.

the longitudinal (x direction), lateral (y direction) and vertical (z direction) harmonic forces (7/rev), respectively. M_{XH}^{7P}, M_{YH}^{7P} and M_{ZH}^{7P} are the rolling (x direction), pitching (y direction) and yawing (z direction) harmonic moments (7/rev), respectively. The results show that the 7/rev forces and moments of the composite blade are much smaller than those of the metal blade.
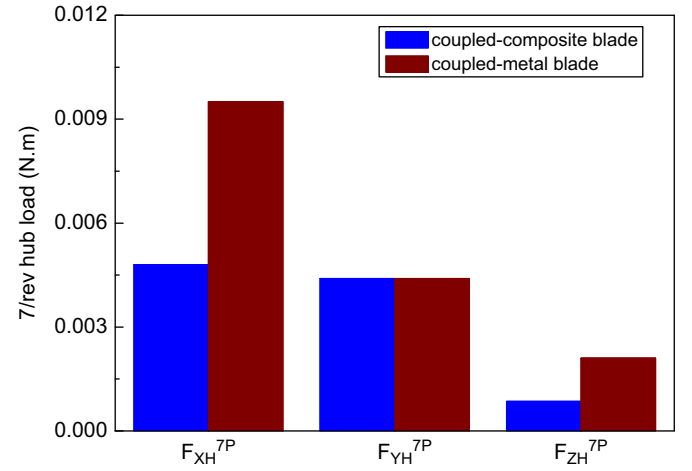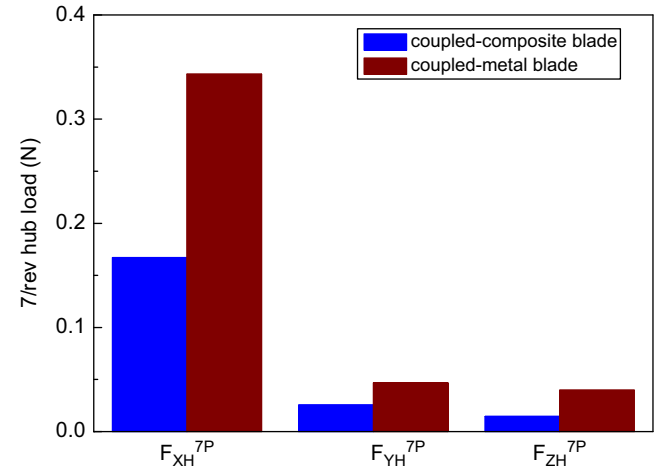

Fig. 19. Comparison of the vibratory hub loads (7/rev) for the composite blade (C1 blade) and the metal blade.

Table 3
Symmetric stacking schemes of the original and modified composite blade.

|	Stacking schemes
C1 blade	$[30_{\overline{2}}/45_{\overline{2}}/0_{\overline{4}}/45_{\overline{6}}/0_{\overline{6}}/45_{\overline{6}}/0_{\overline{6}}\cdots]_s$
C2 blade	$[0_{\overline{2}}/45_{\overline{2}}/0_{\overline{4}}/45_{\overline{6}}/0_{\overline{6}}/45_{\overline{6}}/0_{\overline{6}}\cdots]_s$
C3 blade	$[0_{\overline{2}}/45_{\overline{2}}/90_{\overline{4}}/45_{\overline{6}}/90_{\overline{6}}/45_{\overline{6}}/90_{\overline{6}}\cdots]_s$

3.4. The hydroelastic vibration control

For producing a low vibratory hub loads, in this section, the ply angles and stacking sequences are considered as the design variables. Two improved design propellers (denoted in Table 3 as the C2 blade and the C3 blade), are presented for the composite blade to reduce vibration.

Fig. 20 shows the hydrodynamic load coefficients (per blade) during a rotation in an unsteady flow for different composite blades. It is clear that the thrust and torque load coefficients of the improved composite blades are slightly higher than that of the initially designed composite blade (C1 blade). It can be concluded that the fibre direction of 0 degrees on the surface of blade, compared with the fibre direction of 30 degrees, improves the thrust performance of the highly skewed model propeller.

Fig. 21 presents the vibratory hub loads (7/rev) of the improved and initially designed composite blades. We can see
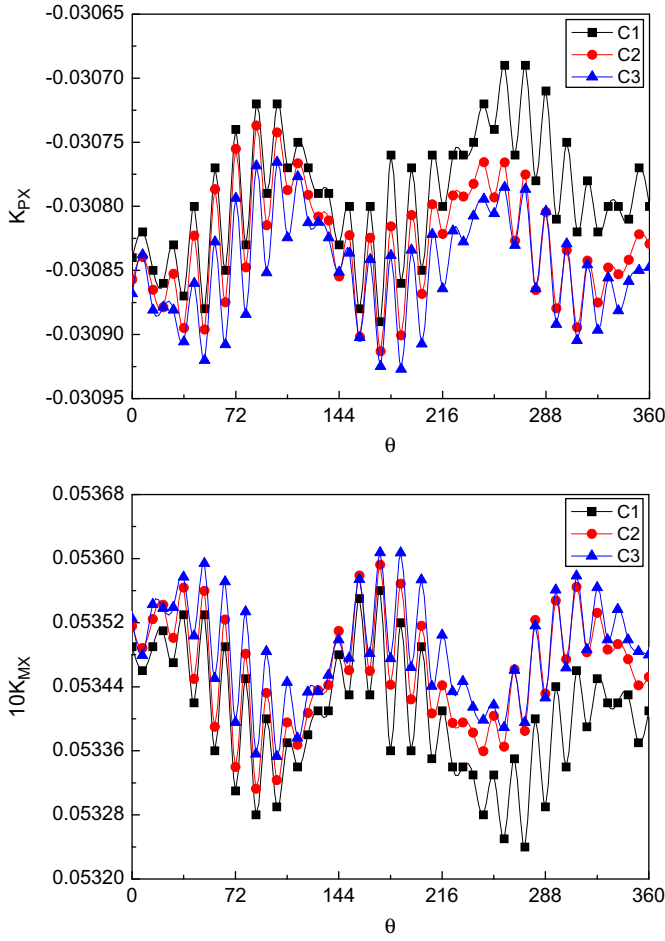
Fig. 20. Comparison of the hydrodynamic load coefficients (per blade) for the initially designed and the improved composite blade in an unsteady flow.

Fig. 21. Comparison of the vibratory hub loads (7/rev) for the initially designed and the improved composite blade.

that there is a reduction of the harmonic force in the *x* direction and the harmonic moment for the improved composite blade, but the harmonic forces in the *y* and *z* directions are slightly higher than that of the initially designed composite blade (C1 blade).
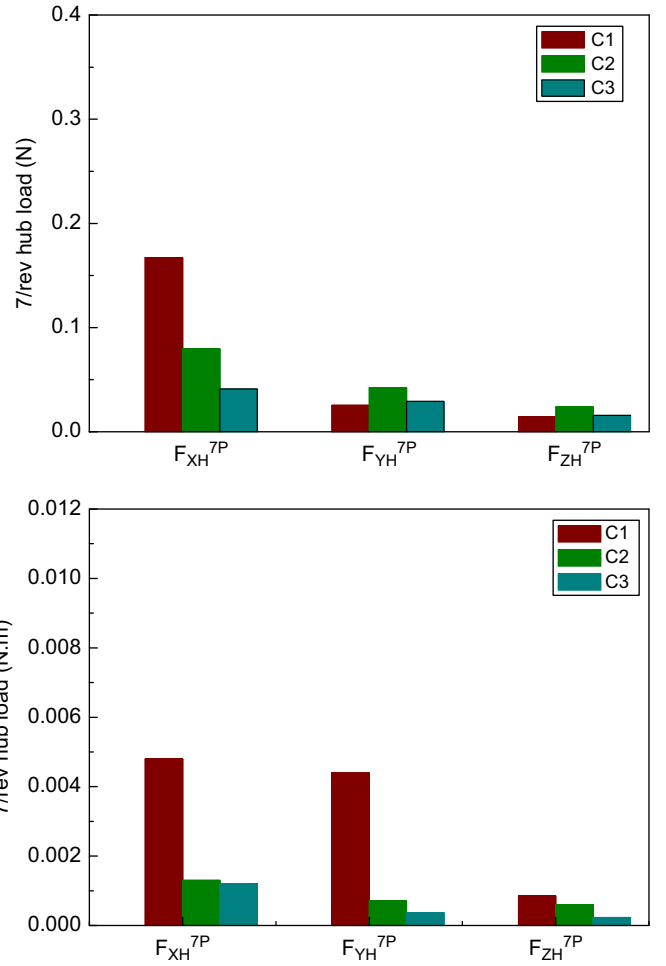
Considering the sum of the scalar norms of the 7/rev harmonic forces and moments as the designed objective function. The formulation of the objective function can be expressed as

$$G = \sqrt{(F_{xF}^{NP})^2 + (F_{yF}^{NP})^2 + (F_{zF}^{NP})^2} + \sqrt{(M_{xF}^{NP})^2 + (M_{yF}^{NP})^2 + (M_{zF}^{NP})^2}$$

where F_{iF}^{NP} and M_{iF}^{NP} ($i=x,y,z$) represent the forces and moments that are nondimensionalised with respect to $\rho n^2 D^4$ and $\rho n^2 D^5$, respectively (Ganguli and Choprat, 1995). The calculated results show that there is a dramatic reduction of nearly 49.6% and 70.6% in the objective function for the improved C2 blade and C3 blade, respectively. This reduction in the vibratory loads is due to a change in the elastic stiffness. Thus, the potential benefit of elastic coupling for vibration control is validated.

4. Conclusions

The hydroelastic phenomena of a highly skewed composite model propeller in an unsteady wake are investigated using a 3-D FEM/CFD coupling algorithm. The added mass and damping matrices are superimposed onto the structural mass and damping matrices, respectively. The nonlinear periodic blade transient responses and vibration hub loads are obtained by solving the coupled equations using the Newton–Raphson numerical procedure. The numerical results are compared with those of a counterpart metal propeller. Additionally, improved composite blades are presented, and vibration control is achieved.

Based on the results, the following conclusions can be drawn:

(1) The 3-D FEM/CFD coupling algorithm is validated for the composite propulsor in unsteady flows.
(2) Because the elasticity of the composite is much greater than that of the metal, the hydroelastic effects of the composite blade are larger than those of the metal blade, i.e., the structural responses of the composite blade are larger than those of the metal blade.
(3) The 7/rev harmonic forces and moments of the composite blade are much smaller than those of the metal blade, which shows the advantage of the composite propeller over a metal blade.
(4) By changing the stacking scheme, the objective function of the vibratory loads dramatically decreases by nearly 49.6% and 70.6% for the improved C2 blade and C3 blade, respectively. The effectiveness of hydroelastic tailoring is demonstrated through the optimisation results.

References

ANSYS, 2009. ANSYS Version 12.0 Documentation.

Duffy, D.G., 2003. Advanced Engineering Mathematics with MATLAB, 2nd ed.

Edward, V.L., 1988. Principles of Naval Architecture Volume II. Resistance, Propulsion and Vibration, second revision. The Society of Naval Architects and Marine Engineers, New Jersey.

Ganguli, R., Choprat, I., 1995. Aeroelastic optimization of a helicopter rotor with composite coupling. J. Aircr. 32 (6), 1326–1334.

Lee, Y.J., Lin, C.C., 2004. Optimized design of composite propeller. Mech. Adv. Mater. Struct. 11, 17–30.

Lin, G.F., 1991a. Comparative Stress-deflection Analyses of a Thick-shell Composite Propeller Blade. Technical Report. David Taylor Research Center, DTRC/SHD-1373-01.

Lin, G.F., 1991b. Three-dimensional stress analyses of a fiber-reinforced composite thruster blade. In: Proceedings of the Symposium on Propellers/Shafting. Society of Naval Architects and Marine Engineers, Virginia Beach, VA, USA.

Lin, H.J., Lin, J.J., 1997. Effect of stacking sequence on the hydroelastic behavior of composite propeller blades. In: Proceedings of the Eleventh International Conference on Composite Materials. Australian Composite Structures Society, Gold Coast, Australia.

Lin, H.J., 2005. Strength evaluation of a composite marine propeller blade. J. Reinf. Plast. Compos. 24, 1791–1807.

Liu, Z., Young, Y.L., 2009. Utilization of bend–twist coupling for performance enhancement of composite marine propellers. J. Fluids Struct. 25, 1102–1116.

Marsh, G., 2004. A new start for marine propellers. Reinf. Plast..

Menter, F.R., 1994. Two-equation eddy-viscosity turbulence models for engineering applications. AIAA-J. 32, 1598–1605.

Mouritz, A.P., Gellert, E., Burchill, P., Challis, K., 2001. Review of advanced composite structures for naval ships and submarines. Compos. Struct. 53, 21–41.

Motley, M.R., Liu, Z., Young, Y.L., 2009. Utilizing fluid–structure interactions to improve energy efficiency of composite marine propellers in spatially varying wake. Compos. Struct. 90, 304–313.

Qing, L.D., 2002. Validation of RANS predictions of open water performance of a highly skewed propeller with experiments. In: Proceedings of the Conference of Global Chinese Scholars on Hydrodynamics.

Taylor, R.L., Beresford, P.J., 1976. A non-conforming element for stress analysis. Int. J. Numer. Methods Eng. 10, 1211–1219.

Van Doormal, J.P., Raithby, G.G., 1984. Enhancement of the SIMPLE method for predicting incompressible fluid flows. Numer. Heat Transfer 7, 147–163.

Watanabe, T., Kawamura, T., Takekoshi, Y., Maeda, M., 2003. Simulation of steady and unsteady cavitations on a marine propeller using a RANS CFD code. In: Proceedings of the Fifth International Symposium on Cavitations.

Young, Y.L., 2008. Fluid–structure interaction analysis of flexible composite marine propellers. J. Fluids Struct. 24, 799–818.